

Application of Convolutional Neural Networks for Extensive Air Shower Separation in the SPHERE-3 Experiment

E. L. Entina^{1*}, D. A. Podgrudkov^{1,2**}, C. G. Azra^{1,2}, E. A. Bonvech¹,
O. V. Cherkasova^{1,3}, D. V. Chernov¹, V. I. Galkin^{1,2}, V. A. Ivanov^{1,2},
T. A. Kolodkin^{1,2}, N. O. Ovcharenko^{1,2}, T. M. Roganova¹, and M. D. Ziva^{1,4}

¹*Skobeltsyn Institute of Nuclear Physics, Lomonosov Moscow State University, Moscow, Russia*

²*Faculty of Physics, Lomonosov Moscow State University, Moscow, Russia*

³*Department of Cosmic Space, Lomonosov Moscow State University, Moscow, Russia*

⁴*Faculty of Computational Mathematics and Cybernetics, Lomonosov Moscow State University, Moscow, Russia*

Received October 1, 2024; revised October 10, 2024; accepted October 20, 2024

Abstract—A new SPHERE-3 telescope is being developed for the study of the cosmic ray spectrum and mass composition in the 5–1000 PeV energy range. Registration of extensive air showers using reflected Cherenkov light method applied in the SPHERE detector series requires a good trigger system for accurate separation of events from the background produced by starlight and airglow photons reflected from the snow. Here, we present the results of convolutional networks application for the classification of images obtained from Monte Carlo simulation of the detector. The simulated detector response includes photon tracing through the optical system, silicon photomultiplier operation, and the electronics response and digitization process. The results are compared to the SPHERE-2 trigger system performance.

Keywords: convolutional neural network, Cherenkov light, cosmic rays

DOI: 10.3103/S0027134924702126

1. INTRODUCTION

Cherenkov light (CL) is the optical component of extensive air showers (EASs) that allows for obtaining some information about the primary particle of the shower and therefore about cosmic rays. For EAS detectors, in order to increase the number of registered EAS events, there is a need to register CL from as large an area as possible. In the case of ground experiments [1–3] this involves an increase in the number of detectors. An alternative is the method of EAS registration which is used in the SPHERE experiment series. The telescope is risen to a certain altitude above the snow surface and detects CL reflected from the snow (Fig. 1). This allows for the use only one compact detector as well as to change the resolution in the energy spectrum sections by changing the telescope altitude. Previous experiments (SPHERE-1 and SPHERE-2) are described in detail in [4].

Comparing to the SPHERE-2 detector, the new one will have a larger aperture and higher spatial resolution (2653 pixels in the light sensitive camera instead of 109), and some other features (like direct EAS CL registration, see [5]). Since the new detector will be carried by an unmanned aerial vehicle, its weight needs to be lower than that of SPHERE-2. The best way to reduce the detector weight is to switch from photomultiplier tubes (PMT) to silicon photomultipliers (SiPM). SiPMs find more and more use in astrophysics applications, specifically in imaging air Cherenkov telescope cameras [6–8], since they are smaller, lighter, and operate at lower voltages than PMTs. Lower operation voltages inherently allow for weight savings in power supply units, which in turn reduces power consumption and further decreases the weight of the batteries.

However, SiPMs have some specific properties that affect measurements: high temperature dependence of both amplification and sensitivity, and optical cross-talk. The former can be resolved by camera and power supply electronics temperature control and

*E-mail: e.l.entina@physics.msu.ru

**E-mail: d.a.podgrudkov@physics.msu.ru

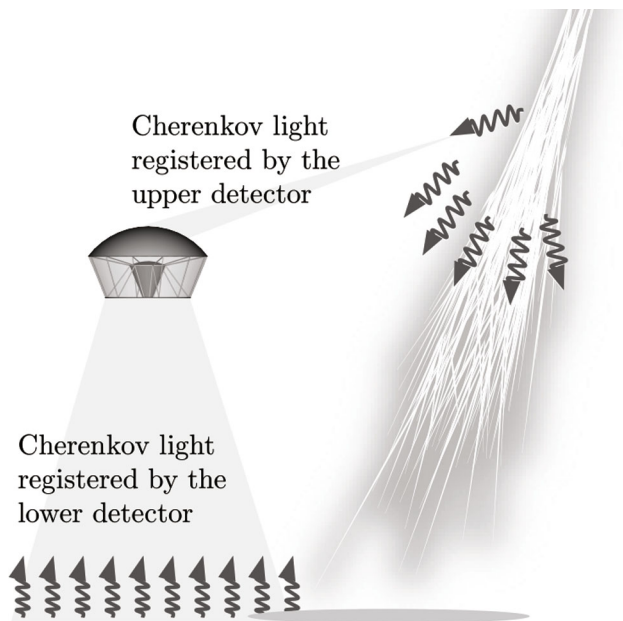


Fig. 1. SPHERE-3 experiment scheme.

stabilization, which is achievable since power consumption and the resulting heat generation are low. The latter, however, should be taken into account in detector design and data analysis. A SiPM is a set of a large number of avalanche photodiodes (individually referred to as microcells) working in Geiger mode that are combined on a single crystal. When a microcell is hit by a photon, it discharges, and this discharge itself can produce optical photons (as any current in a $p-n$ junction does) which can then trigger other microcells in the SiPM. This process is called optical cross-talk (or simply cross-talk in short).

Since the cross-talk is, essentially, a random process and the number of microcells in an individual SiPM is large (from a few hundred to tens of thousands), the actual number of microcells triggered by a single photon and, thus, the resulting response amplitude, is also random. However, while the probability of a cross-talk may be quite high (up to 0.35 and above depending on the SiPM overvoltage), its effect is always an additional signal above the expected and can be accounted for during the calibration and data analysis procedure.

However, for the trigger system, which is needed to separate the signal from the noise (since the telescope is registering light continuously), the situation is different. In the previous version of the telescope, this was done by a topological trigger. Due to the SiPM cross-talk, this approach will not work as intended in the new design.

The rest of the paper is organized as follows: Section 2 describes the trigger system of the previous

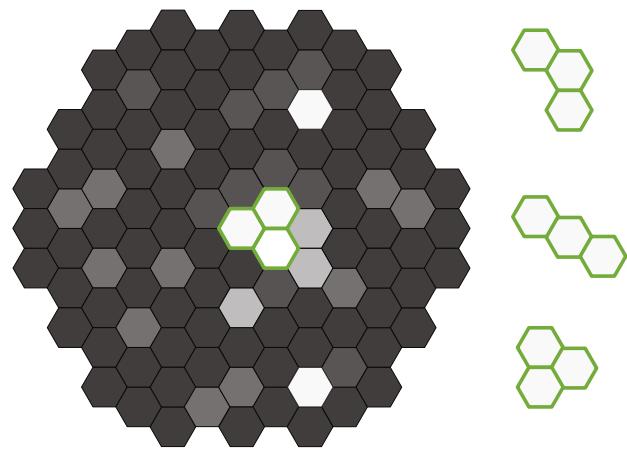


Fig. 2. An example of a topological trigger activation. On the right are shown all possible triplet variations (without rotations).

version of the telescope, and explains the reasons why its direct implementation in the developed telescope is insufficient, and proposes a two-stage model of the trigger algorithm. The following sections of the paper focus on the development of the second trigger stage, namely the additional filtering stage: Section 3 provides information on the solution method, the required data preparation, and the implementation details, Section 4 describes the results, which are then discussed in detail in Section 5.

2. TRIGGER SYSTEM

The SPHERE-2 detector, when triggered, began recording the incoming photon flow. The trigger was topological: first, adaptive thresholds were calculated depending on the noise level (which made the trigger independent of background illumination), after which the topological logic was triggered: if 3 adjacent pixels (Fig. 2) on the mosaic exceeded the threshold within certain time window, recording began.

It is impossible to apply this approach to the new type of pixels. SiPMs are much more susceptible to multiple triggering than PMTs. With an increase in the number of pixels, the number of false triggerings increases due to the larger number of adjacent pixel triplets (which is nearly directly proportional to the number of pixels).

Another issue is that there is a constant flux of background photons and dark current electrons. PMTs by their design cannot produce more than one photoelectron per photon, but have a wide amplification distribution (see, for example, manufacturer or our data [9, 10]). As a result some photons (a few percent) produce a signal amplitude more than twice the average. However, chances of high multiplicity amplitudes are negligible, since the main source of

amplification variation is the number of secondary electrons emitted from first dynode which follows the Poisson distribution. SiPMs have a narrow individual microcell amplification distribution but their cross-talk can cause the signal to be much higher. Studies of SiPMs proposed for use in SPHERE-3 show that chances for high cross-talk multiplicity n are roughly proportional to p^n , where p is the cross-talk probability [11, 12]. This means that for a steady stream of background photons the probability that from a single photoelectron a PMT will produce a pulse 10 times higher than average is below 10^{-30} , while for SiPM with 40% cross-talks this probability is barely around 10^{-4} .

The background photon flux F_b for the SPHERE-3 experiment scheme was estimated to be around 0.04 ph./ns per pixel. With SiPM photon detection efficiency taken into account this gives $F = 0.013$ ph.e./ns. If the SPHERE-2 procedure will be followed, the thresholds setup procedure will set them unacceptably high. The procedure sets the thresholds individually in each pixel in a few passes, every time checking the pixel activation rate and matching it against the target rate. The first is a top to bottom pass, that lowers the initial a priori high threshold by measuring every second the average pixel activation rate. The second pass is individual threshold “tempering,” when each pixel activation frequency should not exceed the target one (an average over 4 s was used), and if it does, the thresholds are increased. The last pass is a general trigger system check, that it does not trigger more often than at a certain rate (1 Hz due to data acquisition system limitations).

The target activation rate for pixels in the SPHERE-2 was $f_t = 100$ Hz. To estimate the number of noise triggerings, the logic of the coincidence method can be applied: for some characteristic time τ (with an accuracy of which it is possible to establish the simultaneity of events) the probability of simultaneous registration of an event by several independent channels depends on the number of these channels. Thus, with $\tau = 1$ μ s coincidence scheme gates the chance of random activation is $f_t\tau$ for a pair of pixels and $(f_t\tau)^2$ for a triplet, respectively. This gives the random trigger rate (for $N_p = 109$ pixels) $N_p f_t^3 \tau^2 \sim 10^{-4}$ Hz, or about once per 3 h, which is significantly higher than required. The SPHERE-2 electronics had low amplification and coarse threshold steps, therefore there was no possible way to lower the thresholds further (e.g., pixel activation rates were either below 1–2 Hz or above 10 kHz).

Application of this logic to SHPERE-3 SiPMs will result in an expected rate of cross-talk multiplicity n per pixel:

$$f(n) = p^n F. \quad (1)$$

This is a simplified approach since cases of simultaneous arrival of 2 or more background photons are ignored. Also cross-talks are treated as simple microcell triggering chains, e.g., a triggered microcell has a chance p to trigger another one, while a correct simulation would be when a triggered microcell has a chance to trigger a number of other microcells with a Poisson mean $\lambda = \ln(1 - p)^{-1}$ (that should also depend on microcell position in the SiPM). The simplified model yields a lower frequency, but the difference is not very significant at higher n (a more accurate probability function can be found in [12]).

For the target rate $f_t = 100$ Hz n should be no less than $\log_p(f/F) + 1 \sim 14$ (it will yield around 10 random triggers per hour). For the target rate $f_t = 1$ kHz n will be about 11 (and about 2.5 random triggers per second). These values are relatively high. SPHERE-2 had 3–5 ph.e. thresholds that worked for big pixels. The small area of a SiPM pixel in the new detector means that fewer signal photons (from EAS) under comparable conditions will hit it, even with respect to the large aperture. This leads to an increase in the energy threshold of the detector. However, the new detector’s target low energy threshold is, again, lower than that of SPHERE-2, thus the number of photons reaching each pixel from an event that should be registered is quite low, on the scale of 3–5.

To solve this problem several options exist. Each has its pros and cons.

Reduction of pixel activated state duration τ will reduce random coincidence rates but can altogether stop the trigger system from activating upon EAS events since they have a time structure measured on the order of microseconds. This includes the time it takes the EAS plane to cross the observation plane plus differences in optical path lengths for different pixels. These values increase with altitude.

Lowering the thresholds by increasing k , which is the number of simultaneously activated pixels required for a trigger to work (random trigger rate is roughly $N_p f_t^k \tau^{k-1}$), will result in a topological complexity in defining which set of pixels is considered adjacent on a hexagonal grid. Moreover, this will increase the number of missed events at lower energies, since a dense patch of pixels will only be activated by bright events, since fluctuations and distribution of the EAS CL photons have a complex structure on the mosaic. In Fig. 3 an example of a signal from an EAS event is shown for reference. The image does not look even remotely smooth.

Implementation of online processing of complex visual patterns will require additional computing power and, critically, more computational time than there reasonably is to make an “an event”/“not an event” trigger decision. This time is no more than 1–4 ticks of the data acquisition system clock or a bit more if some parallelization or data processing conveyor is designed, e.g., 4 parallel processing lanes will give 4 times more time to make a decision, but still this is a very limited time window.

3. METHOD

To circumvent this limitation, it was proposed to use a two-stage trigger system. The idea is that the topological trigger itself is only the first stage of random noise filtration. After it another system checks that there is eventlike data in the buffer. However, it should be noted that this second stage check should be done in a relatively fast manner.

This approach to filtration of random coincidence triggers allows one to ease the overall trigger rate constraints, since there is a limitation only on the overall registration rate (from the data acquisition system operation speed or data storage space limitation). In the first stage, a topological trigger is activated, and a small sample recording begins on a fixed number of bins. The data is then transferred to the second stage designed to filter out fragments without an EAS signal. Thus, the problem of binary classification is addressed.

Operation of the trigger’s second stage requires the identification of complex visual patterns, for what convolutional neural networks (CNNs) [13] were chosen. Subsection 3.1 describes the process of collecting and preparing data for training, and Subsection 3.2 describes the neural network and training parameters.

3.1. Data Preparation

To generate a dataset the process of EAS photons hitting the detector mosaic was simulated. This simulation consisted of 4 stages: generation of a bank of EAS events using the Monte Carlo simulation (with optical background estimation), modeling of the passage of reflected photons through the atmosphere, modeling of the passage of photons through the optical design of the telescope, electronics (SiPM) response calculation.

1. For the Monte Carlo simulation, the CORSIKA [14] package was used. 100 events from 10 PeV primary iron nuclei with the same zenith angle (10°) were simulated. For each simulated event, the coordinates of the shower

Table 1. EAS modeling parameters

Parameter name	Value
Hadron interaction model	QGSJETII-04
Atmosphere model	No.1 (US standard)
Telescope altitude above snow	1000 m
Observation level	450 m
Range of axis coordinates	± 500 m

axis relative to the telescope were also randomly selected 100 times, increasing the number of independent samples to 10 000. Event parameters are given in Table 1.

2. Simulation of the passage of photons from the snow to the detector through the atmosphere involved geometrical reprojecting of the light spot on the snow into a light spot on the entrance aperture of the detector. The Lambertian reflection model for snow was used, which is consistent with the experimental verification of the properties of snow in the previous version of the experiment.
3. For simulation of the passage of photons through the optical design of the telescope, the Geant4 [15] package was used. An optical design with a maximized entrance aperture was selected. The telescope geometry was built using STL files since the mirror and corrector plate was too complex for Geant4 in-built primitives. Configuration parameters are shown in the Table 2.
4. Accounting for electronics involved modeling the response of the data acquisition system to the stream of photons. Since the system at this level is close to linear (operating far from the amplifiers’ limits), the response was calculated as the sum of individual responses to each of the EAS’ and background photons. The response accounts for SiPM cross-talks (parameters were taken from [11] for the same SiPM type—SensL MicroFC-SMTPA-60035 [16]), amplification fluctuations, output pulse profile (see [17]), digitization process (including clock shift across different elements), and more. Electronics simulation parameters are given in Table 3.

The electronics output signal was a 500 bin long ($6.25 \mu\text{s}$) time sequence for each of the 2653 pixels, near the 225 time bin (almost the center) of

Table 2. SPHERE-3 telescope optical system parameters

Parameter name	Value
Curvature radius of the mirror	1654 mm
Mosaic radius	340 mm
Curvature radius of the mosaic	868 mm
Aperture radius	850 mm
Light collector lens radius	7 mm
Entrance aperture area	$\sim 2.27 \text{ m}^2$

Table 3. Electronics response simulation settings

Parameter name	Value
SiPM voltage	29.6 V
SiPM temperature	-15.0°C
SiPM overvoltage	6.02 V
Background photon amplitude	0.013 ph./ns
Digitization frequency	80 MHz

Table 4. Neural network architecture

Layer name	Parameters
Conv2d	(1, 2, 3×3 , 1)
Conv2d	(2, 6, 4×4 , 2)
Conv2d	(6, 3, 4×4 , 2)
Conv2d	(3, 3, 4×4 , 4)
Dense	(345, 2), bias

Table 5. Classification results

		Detected as			
		without threshold		with threshold	
		True	False	True	False
Real label	True	99.3%	0.7%	97.2%	2.8%
	False	1.0%	99.0%	0.1%	99.9%

which was the simulated event. Each pixel (SiPM module) was assigned a serial number, starting from the center, clockwise. The signals from the pixels were combined along one axis in ascending order of the serial number, without additional consideration of positional information. For this 50 bin long non-overlapping fragments (625 ns) were cut out from the

simulated sequence, some containing the full event (since the event location was known), some containing pure background, and each was labelled (Fig. 4). After applying all of the described modifications, the dataset was split into a train and test portions in a ratio of 8 : 2 and normalized. In total the training set contained 8000 samples and the test set contained 2000 samples, both with a 1 : 1 event to background ratio. Then the convolutional neural network was constructed and trained.

Working on prerecorded sections also allows us to use all of the information about a part of the time sequence. This allows us to treat the time dimension as another spatial dimension, and thus use 2D convolutional layers.

3.2. Implementation Details

A practically minimal convolutional neural network architecture was chosen so as to fit if needed onto a microcontroller or FPGA chip. It consisted of 4 convolutional layers and one fully connected layer, as detailed in Table 4. Each cell in the parameters column contains a line ($A, B, C \times D, E$), that should be interpreted as follows: A is the number of input channels, B is the number of output channels, $C \times D$ is the kernel size, E is the stride. The ReLU [18] was used as a nonlinear activation function, and the output layer was normalized using the softmax function, allowing the interpretation of logits as class probabilities.

For training we used the negative log likelihood as a loss function. The Adam optimizer [19] was used with an initial learning rate of 10^{-3} . The CNN was trained for a total of 50 epochs. For validation and evaluation of the final neural network, only accuracy (number of correctly predicted labels) was used.

4. RESULTS

The classification accuracy is given in the Table 5. The critical metric for the two-stage trigger system is the false-positive probability, since during the normal detector operation the event rate is 10^6 times rarer than the expected noise rate. Without any additional manipulations with the outputs the neural network yields a 1.0% false positive rate what is a good result. However, the introduction of class separation thresholds allows for lowering the false positive rate. The separation threshold is an additional constant that is applied to the neural network outputs, artificially inflating or deflating the probability of predicting a specific class. Fine-tuning this value allows one to achieve maximum filtering with an acceptable number of missed events. In Table 5 the “without threshold” columns show the metrics for the pure outputs

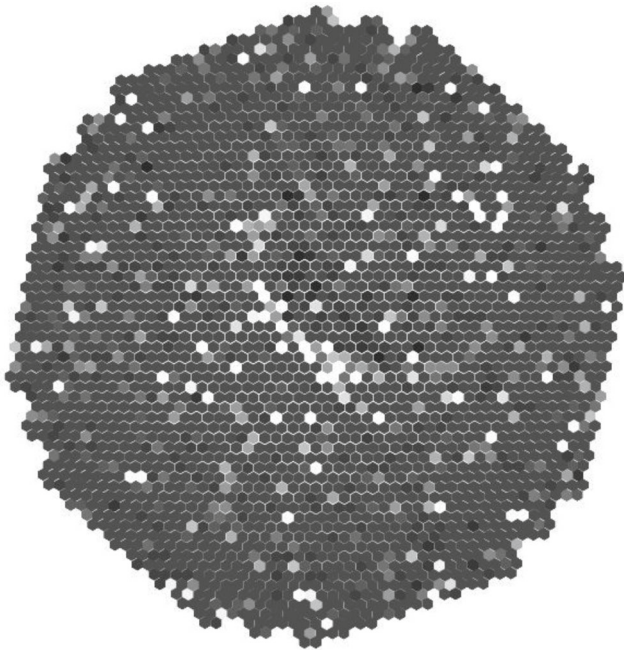


Fig. 3. Example of an EAS CL structure on the mosaic from a primary 10 PeV iron nuclei. The image represents some instant signal values in pixels and not the total signal collected. The crescent shape of EAS is the result of photon arrival delays due to differences in optical path lengths.

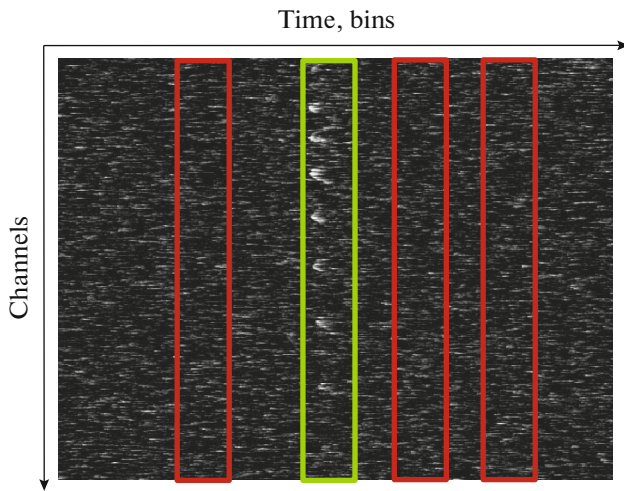


Fig. 4. Dataset preparation step. The red highlighted areas contain only noise, and the green highlighted area contains the EAS-event signal.

of the neural network. The “with threshold” columns show the results with class separation threshold applying.

By adjusting the class separability threshold, the number of false positives can be reduced to 0.1%, albeit at the cost of losing 2.8% of events (false negative rate).

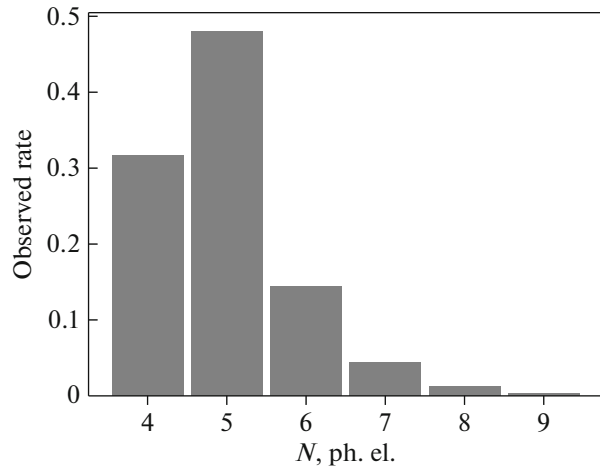


Fig. 5. Distribution of the third pixel amplitude in the brightest triplet of the EAS image.

5. DISCUSSION

The comparison with SPHERE-2 was carried out in a somewhat complex manner. The energy threshold of the SPHERE telescopes depends on the altitude (nearly linearly). The majority of the SPHERE-2 flights were carried out at an altitude of around 480–500 m. The estimated energy threshold for this altitude was around 10 PeV (see Subsection 5.2 in [4] for details). The expected SPHERE-2 energy threshold for 1000 m altitude would have been around 20 PeV.

Simulations for SPHERE-3 in this work showed that 10 PeV EAS rarely produce amplitudes corresponding to 14 photoelectrons in the third brightest pixel of the whole event. However, in 50% of the cases the dimmest pixel of the brightest triplet had around 5 photoelectrons (see Fig. 5). This means that direct application of the SPHERE-2 logic to the SPHERE-3 detector (as described in Section 2) would lead to an energy threshold of above 30 PeV (since EAS CL flux is proportional to primary energy). The 0.1% false positive rate of the neural network obtained in the previous section allows achieving a 10^3 times higher rate of trigger activation. This pixel activation rate corresponds to a 6–7 photoelectrons amplitude (e.g., almost two times lower) and around 12–15 PeV detector energy threshold.

Precision of the primary particle parameters reconstruction in case of such low signal amplitudes is a matter of another study, however, the large number of pixels allows one to use statistical approaches for data analysis and further detector operation optimization. Additionally, the possibility of implementing a neural network using the limited computational power of FPGA chips or microcontrollers has not yet been fully explored, as no specific solutions have been selected for the implementation of the detector electronics.

Other approaches to the trigger system logic (shorter pixel activation time, switching from triplets to septets, etc.) will be also studied for their effective energy thresholds. It also should be kept in mind, that this study was performed for reflected EAS CL that has a relatively long-time structure. The option of direct CL registration by the main telescope camera was not included in the scope of this study, as it has different temporal properties. However, for its case the trigger system should also account for short bright bursts of direct CL as a factor of operation.

ACKNOWLEDGMENTS

The research was carried out using the equipment of the shared research facilities of HPC computing resources at Lomonosov Moscow State University [20].

FUNDING

This work is supported by the Russian Science Foundation, grant no. 23-72-00006 (<https://rscf.ru/project/23-72-00006/>).

CONFLICT OF INTEREST

The authors of this work declare that they have no conflicts of interest.

REFERENCES

1. D. V. Chernov, E. E. Korosteleva, L. A. Kuzmichev, V. V. Prosin, I. V. Yashin, N. M. Budnev, O. A. Gress, T. I. Gress, L. V. Pankov, Yu. V. Parfenov, Yu. A. Semenev, B. K. Lubsandorzhiev, P. G. Pokhil, T. Schmidt, Ch. Spiering, and R. Wischnewski, *Int. J. Mod. Phys. A* **20**, 6799 (2005).
<https://doi.org/10.1142/S0217751X05030120>
2. A. K. Alekseev, E. A. Atlasov, N. G. Bolotnikov, A. V. Bosikov, N. A. Dyachkovskiy, N. S. Gerasimova, A. V. Glushkov, A. A. Ivanov, O. N. Ivanov, D. N. Kardashevsky, I. A. Kellarev, S. P. Knurenko, A. D. Krasilnikov, A. N. Krivenkov, I. V. Ksenofontov, L. T. Ksenofontov, K. G. Lebedev, S. V. Matarkin, V. P. Mokhnachevskaya, E. V. Nikolaeva, N. I. Neustroev, I. S. Petrov, N. D. Platonov, A. S. Proshutinsky, A. V. Saburov, I. Ye. Sleptsov, G. G. Struchkov, L. V. Timofeev, and B. B. Yakovlev, *Phys. At. Nucl.* **84**, 893 (2021).
<https://doi.org/10.1134/S1063778821130020>
3. S. N. Vernov, G. B. Khristiansen, V. B. Atrashkevich, et al., in *Proc. of the 16th Int. Cosm. Rays Conf.* (Kyoto, Japan, 1979), Vol. 8, p. 129.
4. R. A. Antonov, T. V. Aulova, E. A. Bonvech, V. I. Galkin, T. A. Dzhatdov, D. A. Podgrudkov, T. M. Roganova, and D. V. Chernov, *Phys. Part. Nucl.* **46**, 60 (2015).
<https://doi.org/10.1134/S1063779615010025>
5. E. A. Bonvech, D. V. Chernov, V. S. Latypova, C. Azra, V. I. Galkin, V. A. Ivanov, D. A. Podgrudkov, and T. M. Roganova, *Bull. Russ. Acad. Sci.: Phys.* **88**, 435 (2024).
<https://doi.org/10.1134/S1062873823705676>
6. D. Dorner, M. L. Ahnen, M. Bergmann, A. Biland, M. Balbo, T. Bretz, J. Buss, S. Einecke, J. Freiwald, C. Hempling, D. Hildebrand, G. Hughes, W. Lustermaan, K. Mannheim, K. Meier, S. Mueller, D. Neise, A. Neronov, A.-K. Overkemping, A. Paravac, F. Paus, W. Rhode, T. Steinbring, F. Temme, J. Thaele, S. Toscano, P. Vogler, R. Walter, and A. Wilbert, *arXiv Preprint* (2015).
<https://doi.org/10.48550/arXiv.1502.02582>
7. C. Arcaro, M. Doro, J. Sitarek, and D. Baack, *Astropart. Phys.* **155**, 102902 (2024).
<https://doi.org/10.1016/j.astropartphys.2023.10-2902>
8. L. P. Taylor et al. (on behalf of the CTA SCT Project), *Proc. Sci.* **395**, 748 (2021).
<https://doi.org/10.22323/1.395.0748>
9. R. A. Antonov, E. A. Bonvech, D. V. Chernov, D. A. Podgrudkov, and T. M. Roganova, *Astropart. Phys.* **77**, 55 (2016).
<https://doi.org/10.1016/j.astropartphys.2016.01.004>
10. Hamamatsu Photonics K.K., *Photomultiplier Tubes: Basics and Applications*, 4th ed. (2017).
11. A. A. Amineva, A. V. Pantiukhin, and D. A. Podgrudkov, *Uchenye Zapiski Fizicheskogo Fakul'teta MGU*, No. 4, 2341602 (2023).
12. F. Rehbein, T. Bretz, A. Biland, R. Alfaro, J. Audehm, G. Do, M. M. González, Y. F. Pérez Araujo, M. Schaufel, J. Serna-Franco, and I. Torres, *Rev. Mex. Astron. Astrofis.* **59**, 379 (2023).
<https://doi.org/10.22201/ia.01851101p.20-23.59.02.14>
13. Y. LeCun, K. Kavukcuoglu, and C. Farabet, in *Proceedings of 2010 IEEE International Symposium on Circuits and Systems, Paris, 2010* (IEEE, 2010), p. 253.
<https://doi.org/10.1109/ISCAS.2010.5537907>
14. D. Heck, J. Knapp, J. N. Capdevielle, G. Schatz, and T. Thouw, *CORSIKA: A Monte Carlo code to simulate extensive air showers*, Technical Report FZKA-6019 (Forschungszentrum Karlsruhe, Karlsruhe, 1998).
<https://digbib.bibliothek.kit.edu/volltexte/fzk/60-19/6019.pdf>
15. S. Agostinelli, J. Allison, K. Amako, J. Apostolakis, H. Araujo, P. Arce, M. Asai, D. Axen, S. Banerjee, G. Barrand, F. Behner, L. Bellagamba, J. Boudreau, L. Broglia, A. Brunengo, H. Burkhardt, S. Chauvie, J. Chuma, R. Chytrcek, G. Cooperman, G. Cosmo, P. Degtyarenko, A. Dell'Acqua, G. Depaola, D. Dietrich, R. Enami, A. Feliciello, C. Ferguson, H. Fesefeldt, G. Folger, F. Foppiano, A. Forti, S. Garelli, S. Giani, R. Giannitrapani, D. Gibin, J. J. Gómez

- Cadenas, I. González, G. Gracia Abril, G. Greeniaus, W. Greiner, V. Grichine, A. Grossheim, et al., Nucl. Instrum. Methods Phys. Res., Sect. A **506** (3), 250 (2003).
[https://doi.org/10.1016/S0168-9002\(03\)01368-8](https://doi.org/10.1016/S0168-9002(03)01368-8)
16. ON Semiconductors, Silicon photomultipliers (SiPM), low-noise, bluesensitive (2020).
<https://www.onsemi.com/pdf/datasheet/microc-series-d.pdf>.
17. D. V. Chernov, C. G. Azra, E. A. Bonvech, V. I. Galkin, V. A. Ivanov, V. S. Latypova, D. A. Podgrudkov, and T. M. Roganova, Phys. At. Nucl. **85**, 641 (2023).
<https://doi.org/10.1134/S1063778822060059>
18. V. Nair and G. E. Hinton, in *Proceedings of the 27th International Conference on Machine Learning (ICML-10)* (2010), p. 807. <http://www.cs.toronto.edu/fritz/absps/reluICML.pdf>.
19. D. P. Kingma and J. Ba, arXiv Preprint (2014).
<https://doi.org/10.48550/arXiv.1412.6980>
20. V. V. Voevodin, A. S. Antonov, D. A. Nikitenko, P. A. Shvets, S. I. Sobolev, I. Yu. Sidorov, K. S. Stefanov, V. V. Voevodin, and S. A. Zhumatiy, Supercomputing Frontiers and Innovations **6** (2), 4 (2019).
<https://doi.org/10.14529/jsfi190201>

Publisher's Note. Allerton Press, Inc. remains neutral with regard to jurisdictional claims in published maps and institutional affiliations.

AI tools may have been used in the translation or editing of this article.